Volume 1 | Number 1 | Jan 2013 | Pages 1–100

PCCP

Physical Chemistry Chemical Physics
www.rsc.org/pccp

ROYAL SOCIETY OF CHEMISTRY

ROYAL SOCIETY OF CHEMISTRY

www.rsc.org/pccp

Graphical Abstract

Synergistic contributions by decreasing overpotential and enhancing charge-transfer in α-Fe$_2$O$_3$/Mn$_3$O$_4$/graphene catalysts with heterostructures for photocatalytic water oxidation

Shunli Yin[a], Xiaomei Wang[b], Zhigang Mou[a], Yijie Wu[a], Hui Huang[a], Mingshan Zhu[c], Yukou Du[a], Ping Yang[*a]

[a.] College of Chemistry, Chemical Engineering and Materials Science, Soochow University, Suzhou 215123, [b.] College of Chemistry and Bioengineering, Suzhou University of Science and Technology, Suzhou 215011, [c.] CAS Key Laboratory of Colloid, Interface and Chemical Thermodynamics Institute of Chemistry, Chinese Academy of Sciences, Beijing 100190, China

E-mail address: pyang@suda.edu.cn

Graphical Abstract:

Proposed mechanism of oxygen evolution from α-Fe$_2$O$_3$/Mn$_3$O$_4$-1/rGO-3 photocatalyst.

Physical Chemistry Chemical Physics

ARTICLE TYPE
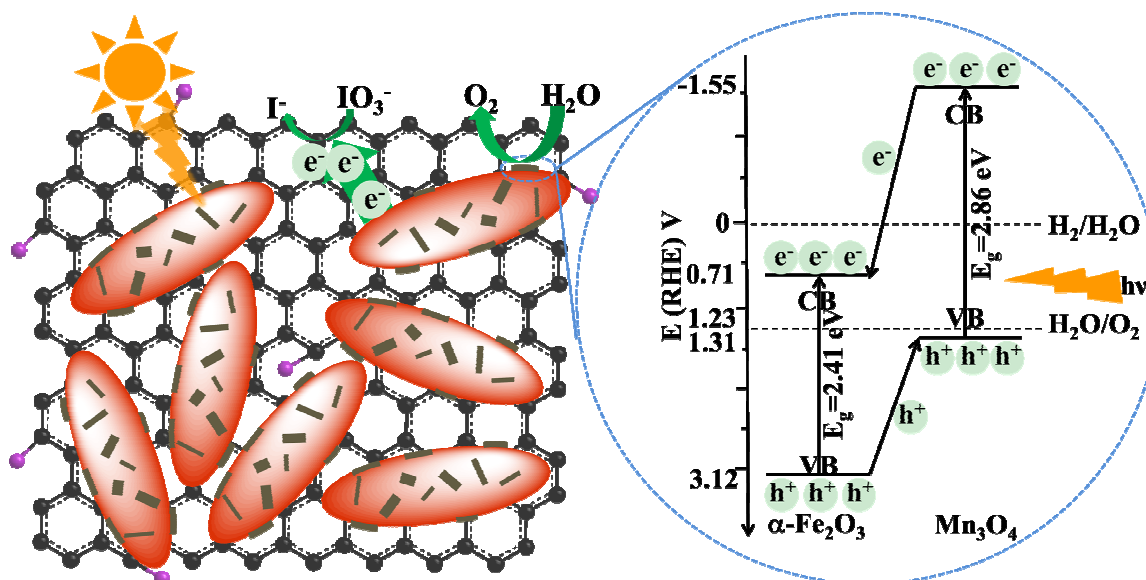
Synergistic contributions by decreasing overpotential and enhancing charge-transfer in α-Fe₂O₃/Mn₃O₄/graphene catalysts with heterostructures for photocatalytic water oxidation†

Shunli Yin[a], Xiaomei Wang[b], Zhigang Mou[a], Yijie Wu[a], Hui Huang[a], Mingshan Zhu[c], Yukou Du[a], Ping

5 **Yang[*a]**

A novel nanocomposite consisted of α-Fe₂O₃, Mn₃O₄ and reduced graphene oxide (r-GO) has been facilely synthesized through a two-step method: solvothermal reaction for Mn₃O₄-modified α-Fe₂O₃ (α-

10 Fe₂O₃/Mn₃O₄) and self-assembly process for combining α-Fe₂O₃/Mn₃O₄ with r-GO (α-Fe₂O₃/Mn₃O₄/r-GO). The morphology and structure of the nanocomposite were characterized by X-ray diffraction (XRD), scanning electron microscopy (SEM), high-resolution transmission electron microscopy (HRTEM) and X-ray photoelectron spectroscopy (XPS). The results demonstrated that the rod-like hematite was modified by Mn₃O₄ and dispersed on the surface of r-GO. Raman and Fourier transform

15 infrared spectra (FTIR) showed superior interfacial contacts between α-Fe₂O₃/Mn₃O₄ and r-GO. Ultraviolet-visible diffuse reflectance spectroscopy (DRS) and photoelectrochemical characterizations revealed a high light-harvesting efficiency, a lowered overpotential for water oxidation and an excellent charge transfer performance of α-Fe₂O₃/Mn₃O₄/r-GO nanocomposite with heterostructures. The photocatalytic oxygen evolution from the optimized photocatalyst was up to 1406.2 μmol g⁻¹ in 10 h UV-

20 vis light irradiation and the quantum yield was ca. 4.35 % at 365 nm. Our investigation suggests that constructing a catalyst with heterostructures is a promising method to enhance photocatalytic activity.

1. Introduction

Semiconductor-based photocatalysts have attracted great attention owing to their potential applications in the field of
25 converting solar energy to chemical fuel.[1] Over the past several decades, the researches on semiconductor-based photocatalytic hydrogen generation through water splitting have achieved a significant progress.[2-4] Because all attractive technologies for solar-powered hydrogen production involve multi-electron
30 oxidation of water, which is more difficult due to thermodynamic and kinetic limitations, thus, more attentions should be focused on the water oxidation reaction.[5-7] The interest in this process carried out by semiconductor-based photocatalysts has increased,[8-12] but the photo-activities of the catalysts are still
35 weak. One of important factors affecting the photocatalytic activities is the high overpotential of the catalysts.[13, 14] Introducing co-catalysts such as noble metals (e.g. Pt and Pd) or noble metal oxides (e.g. RuOₓ and IrOₓ) onto the surface of the semiconductor-based catalysts is an efficient strategy to
40 overcome the drawback.[15-20]

Hematite (α-Fe₂O₃) as an environment friendly material can be obtained easily and is stable enough in neutral or alkaline solutions.[21-24] In addition, hematite is a solar-active n-type

semiconductor with a narrow band gap (ca. 2.1-2.2 eV),[25, 26] and
45 has been used as catalysts for various photocatalytic or photoelectrocatalytic reactions.[27-31] However, the promise of hematite as a photo- or photoelectro- catalyst for water oxidation is still debated in latest decades for its some intrinsic defects, including relatively large overpotential, poor majority carrier
50 conductivity and short diffusion length of minority carrier (L_D = 2-4 nm).[32-34] Various methods have been devoted to overcome these issues. Feng's group reported a novel hematite-based nanocomposite for photoelectrochemical water splitting under visible light irradiation.[35] The nanocomposite demonstrated
55 enhanced catalytic activity because the overpotential of hematite was reduced by the surface modification.[36] Hisatomi and co-workers also reported that ultrathin hematite photoanode demonstrated enhanced photocatalytic activity for water splitting to produce oxygen since the mobility of the photoexcited carriers
60 in the ultrathin hematite photoanode increased.[37] However, new and efficient photocatalysts with low overpotential and increasing charge-transfer ability are still needed in order to meet requirement of solar energy conversion.

In recent years, hausmannite (Mn₃O₄) as one of mixed
65 valence manganese oxides has been employed as a co-catalyst to build novel semiconductor composites for photocatalysis. These

composite photocatalysts exhibited higher performance since Mn_3O_4 nanoparticles in the composites acted as O_2 evolution promoters.[38] As is well known, graphene as a new block to construct light-harvesting assemblies has stimulated great research interest in the solar-energy conversion field due to its high charge carrier mobility, outstanding optical property, huge specific surface area and great mechanical strength.[39-41] Many new photoelectrocatalytic or photocatalytic materials using graphene as an important component have been designed and synthesized. [42, 43]

In this paper, we report a facile method to synthesize a novel nanocomposite composed of α-Fe_2O_3, Mn_3O_4 and reduced graphene oxide (r-GO) for photocatalytic water oxidation to producing oxygen. The typical p-type semiconductor Mn_3O_4 in the nanocomposite forms a heterojunction with α-Fe_2O_3 enhancing the charge transfer. In addition, Mn_3O_4 also acts as a noble-metal free co-catalyst reducing oxygen evolution overpotential of hematite. Reduced graphene oxide in the nanocomposite serves not only as a superior supporting matrix for anchoring the semiconductor nanoparticles but also as an excellent electron mediator to adjust electron transfer. The nanocomposite exhibited remarkable enhanced photocatalytic activity toward water oxidation compare with bare hematite or α-Fe_2O_3/Mn_3O_4 under UV-vis light irradiation. The quantum efficiency of the optimized photocatalyst was up to 4.35 % at 365 nm. The photocatalysts also displayed excellent stability during the photoreaction. Our investigation proposes that constructing a catalyst with heterostructures is an efficient method to enhance photocatalytic activity.

2. Experimental

2.1. Sample synthesis

Graphene oxide (GO) was prepared with a modified Hummers method from graphite powders,[44] and reduced graphene oxide (r-GO) was prepared according to the method reported by Zhou and co-workers.[45] In detail, 50 mL of 2 mg mL^{-1} GO ethanol suspension with brown color was transferred to a 65 mL Teflon-lined autoclave, heated at 180 °C for 6 h in an oven, and cooled to room temperature. The black solid sample was collected by filtered, washed with deionized water three times, and dried at 80 °C in vacuum overnight. Lastly, 10 mg of the obtained solid was dispersed into 100 mL of deionized water and bath-sonicated for 120 min, resulting stable r-GO colloidal suspension (0.1 mg mL^{-1}).

The nanorods of α-Fe_2O_3 were synthesized based on the reported hydrothermal method.[46] In a typical procedure, 2.0 mL of $FeCl_3$ solution (0.5 M) and 1.8 mL of NaH_2PO_4 solution (0.02 M) were mixed with 46 mL distilled water under vigorous stirring. The mixture was transferred into a 65 mL Teflon-lined stainless-steel autoclave and was heated in an oven at 220 °C for 2 h. The red solid was obtained by centrifugation, washed with distilled water and ethanol, and dried at 80 °C in vacuum overnight. Finally, the sample was calcined at 400 °C for 3 h in air for better crystallization.

The Mn_3O_4 modified α-Fe_2O_3 hybrid was prepared by a surfactant-free solvothermal strategy.[47, 48] Typically, 30 mg of α-Fe_2O_3 powders and 0.68 mL of $Mn(Ac)_2$ alcohol solution (5.8 ×

10^{-3} M) were mixed with 50 mL of ethanol, and stirred vigorously for 10 min. Then, the suspension was transferred into a 65 mL Teflon-lined stainless autoclave and heated at 120 °C for 24 h. The solid sample was collected by centrifugation, washed with ethanol for several times, and dried at 50 °C for 2 h in a vacuum oven. Changing the ratio of the starting materials, the hybrids in different composition can be prepared. The as-prepared sample is designated as α-Fe_2O_3/Mn_3O_4-x, where x stands for the weight percent of Mn_3O_4 to α-Fe_2O_3 in the hybrid.

The nanocomposite composed of α-Fe_2O_3, Mn_3O_4 and r-GO was prepared by a self-assembly process.[3, 49, 50] In a typical experiment, 10 mg of α-Fe_2O_3/Mn_3O_4-1 and 3 mL of r-GO colloidal (0.1 mg mL^{-1}) were added into 47 mL of deionized water under magnetic stirring. The pH value of the system was adjusted to 3 by adding diluted hydrochloric acid solution. The stirring was kept for 12 h at room temperature. The solid was collected by centrifugation, washed with deionized water for several times, and dried at 50 °C overnight in a vacuum oven. The sample is designated as α-Fe_2O_3/Mn_3O_4-x/r-GO-y, where y stands for the weight percent of r-GO to α-Fe_2O_3 in the nanocomposite.

2.2. Characterization

The X-ray diffraction measurements were carried out on a Philips diffractometer equipped with Ni-filtered Cu Kα radiation to obtain the structure and crystalline phase composition of samples. The spectra were collected in reflection geometry at 2θ-values ranging from 20 to 70°. Scanning electron microscopy (SEM) measurements were performed on SEM Hitachi S-4800. High-resolution transmission electron microscope (HRTEM) images were obtained using a TECNAI-G20 electron microscope operating at an accelerating voltage of 200 kV. X-ray photoelectron spectroscopy (XPS) measurements were taken by an AXIS Ultra DLD system (Kratos Analytical Inc.) using monochromatic Al Kα radiation. Binding energies were calculated with respect to C (1s) at 284.6 eV. The ultraviolet-visible diffuse reflectance spectrometry was recorded with a Hitachi UV-3010 spectrophotometer using $BaSO_4$ as a reference. Fourier transform infrared (FTIR) spectra were obtained with a Thermo Scientific Nicolet 6700 instrument. Raman measurements were performed on a Jobin Yvon HR-800 spectrometer (λ = 633 nm).

2.3. Photoelectrochemical measurements

The measurements of photoelectrical response were carried out on a CHI660D potentiostat/galvanostat electrochemical analyser in a three-electrode system, which consisting of an indium tin oxide (ITO) conductive glass covered with a sample as the working electrode, a platinum wire as counter electrode and a saturated calomel electrode (SCE) as reference electrode. The electrodes were immersed in a Na_2SO_4 aqueous solution (0.2 M, pH ~ 6). The working electrode was irradiated by UV-visible light from a GY-10 xenon lamp (150 W) during the measurement. For converting the obtained potential (vs. SCE) to reversible hydrogen electrode (RHE), the following Nernst equation was used:

$$E_{RHE} = E_{SCE} + 0.059\text{pH} + E^{\circ}_{SCE}$$

where E_{RHE} is the converted potential vs. RHE, E_{SCE} is the experiment value of potential vs. SCE, and E°_{SCE} = 0.2415 V at

25 °C.[51]

The electrochemical impedance spectroscopy (EIS) displayed as Nyquist plot was carried out in the frequency range of 10^{-1} to 10^5 Hz with alternating current (AC) voltage amplitude of 5 mV at direct current (DC) bias of 0.5 V vs. SCE. The Mott-Schottky (M-S) plots were measured with a frequency of 1000 Hz under UV-visible light irradiation. The DC potential was kept in the range from -0.2 to 1.0 V vs. SCE for hematite and from 0.5 to 1.1 V vs. SCE for Mn_3O_4. The Mott-Schottky equation was used to calculate the flat-band potential (E_{fb}) of the semiconductors:

$$1/C^2 = 2/e\varepsilon\varepsilon_0 N_d \times (E - E_{fb} - kT/e)$$

where C is the capacitance of the electrode, e is the elementary charge, ε is the dielectric constant of the electrode material, ε_0 is permittivity of vacuum, E is the applied potential, k is the Boltzmann constant and T is the temperature. E_{fb} is derived by the intercept of the potential axis, which obtained by extrapolating the linear region of the plot.[52]

The optical band gap of semiconductors was determined by the following Tauc equation:

$$\alpha h v = A(h v - E_g)^n$$

where $h v$ is the photon energy, E_g is the optical band gap energy, α is measured absorption coefficient, A and n are constant. For the direct and indirect band gap, the value of n is 0.5 and 2, respectively. E_g is estimated by the intercept of the photon energy axis, which obtained by extrapolating the linear region of the plot.[53]

2.4. Photocatalytic oxygen evolution reaction

The photocatalytic reaction was carried out in a 50 mL quartz flask equipped with a flat optical entry window. Typically, 5 mg of the photocatalyst and 5.4 mL of KIO_3 aqueous solution (9.3×10^{-3} M) were added into 45 mL of deionized water. The system was deaerated by bubbling argon (Ar) into the solution for 1 h. The system was irradiated with a GY-10 xenon lamp (150 W, I_0 = 3550 μw cm^{-2} at 365 nm; I_0 = 14500 μw cm^{-2} at 420 nm) at 298 K. The distance between the flat optical window of the flask and the lamp was 10 cm. The evolved oxygen was detected by an online gas chromatograph (GC1690) armed with a thermal conductivity detector (TCD) and a couple of 5 Å molecular sieve columns using Ar as carrier gas. The GC signal was calibrated by standard O_2/Ar gas mixtures of known concentrations.

3. Results and discussion

3.1. Morphology and structure of the samples

The phase purity and crystal structure of the samples were investigated by X-ray diffraction (Fig. 1). The characteristic peaks at 23.5°, 32.0°, 34.4° and 61.5° (Fig. 1, curve a) are corresponding to the (012), (104), (110) and (300) crystalline planes of hematite, respectively, demonstrating that hematite has been obtained through hydrothermal process.[48, 54] After calcination at 400 °C for 3 h, the diffraction intensity at 34.4° and 61.5° reinforced, indicating better crystallinity of hematite (Fig. 1, curve b).[55] For α-Fe$_2$O$_3$/Mn$_3$O$_4$-1 hybrid and α-Fe$_2$O$_3$/Mn$_3$O$_4$-1/r-GO-3 nanocomposite, characteristic peaks of Mn_3O_4 and r-GO are not observed in the patterns (Fig. 1, curve c and d), which may be attributed to the low content and high dispersion of Mn_3O_4 and r-GO in the samples.[4] The FTIR spectra of r-GO and α-Fe$_2$O$_3$/Mn$_3$O$_4$-1/r-GO-3 nanocomposite are shown in Fig. S1.

For the r-GO sample (Fig. S1, curve a), the band at 1382 cm^{-1} is corresponding to the typical vibration peak of graphene.[56] The other band centred at 1400 cm^{-1} is contributed to antisymmetry stretching of the C-O bond from COOH groups in r-GO.[4, 57] The relative weak intensity of the peak indicates that the GO has been reduced in the hydrothermal process.[4] For the α-Fe$_2$O$_3$/Mn$_3$O$_4$-1/r-GO-3 sample (Fig. S1, curve b), both of the typical peaks of r-GO can be observed demonstrating the presence of r-GO in the nanocomposite.[50]
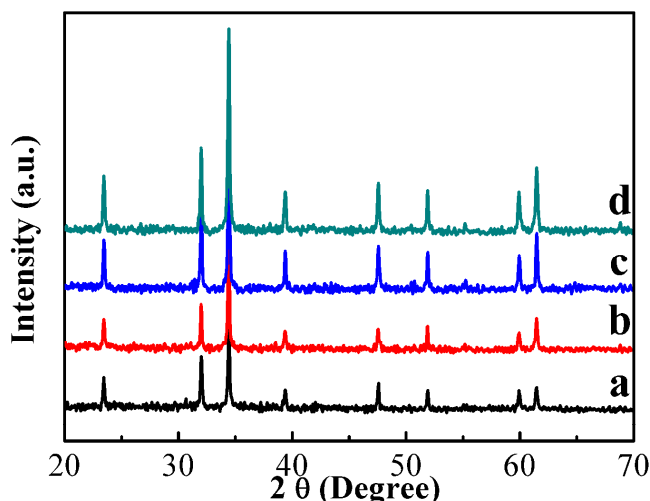

Fig. 1 XRD patterns of (a) α-Fe$_2$O$_3$, (b) α-Fe$_2$O$_3$ calcined under 400 °C, (c) α-Fe$_2$O$_3$/Mn$_3$O$_4$-1 and (d) α-Fe$_2$O$_3$/Mn$_3$O$_4$-1/r-GO-3.

The Raman spectra of r-GO and α-Fe$_2$O$_3$/Mn$_3$O$_4$-1/r-GO-3 are shown in Fig. S2. The strong peak centred at 1333 cm^{-1} representing the defected-induced vibration of C-C band is the typical D band of r-GO; and the weak peak centred at 1598 cm^{-1} relating to the vibration of sp^2 C-C band is corresponding to the G band (Fig. S1, curve a).[3] The largish value of relative intensity ratio of D to G band (I_D/I_G) displays that the size of graphene sheet is comparatively small.[40] For the sample of α-Fe$_2$O$_3$/Mn$_3$O$_4$-1/r-GO-3 (Fig. S1, curve b), the G band position of r-GO negative-shift ca. 2 cm^{-1} provides reliable evidence of the superior interactions between α-Fe$_2$O$_3$/Mn$_3$O$_4$ hybrid and r-GO in the nanocomposite.[3, 58]
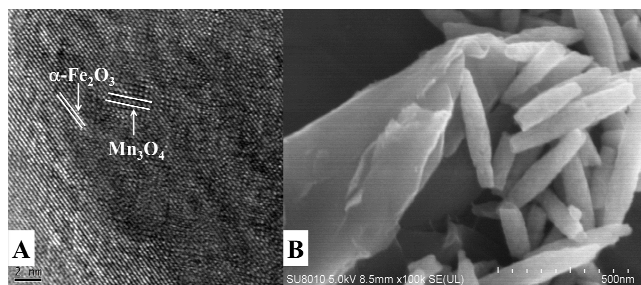

Fig. 2 (A) HRTEM image of α-Fe$_2$O$_3$/Mn$_3$O$_4$-1 hybrid and (B) SEM image of α-Fe$_2$O$_3$/Mn$_3$O$_4$-1/r-GO-3 nanocomposites.

The as-prepared hematite demonstrates a rod-like shape with a diameter of ca. 100 nm and a length of ca. 400 nm (Fig. S3A) and the calcination at 400 °C does not change the morphology of hematite obviously (Fig. S3B). Two entirely different types of

lattice spacing, 0.251 nm for (110) plane of hematite and 0.420 nm for (220) plane of Mn_3O_4,[59, 60] are surveyed in the HRTEM image of α-Fe_2O_3/Mn_3O_4-1, indicating that α-Fe_2O_3 has been decorated with nanoscale Mn_3O_4 (Fig. 2A). The SEM image of α-Fe₂O₃/Mn₃O₄/r-GO nanocomposite demonstrates that α-Fe_2O_3/Mn_3O_4 rods are well scattered on the wrinkles surface of r-GO sheets (Fig. 2B).

The XPS analysis is used to reveal the surface chemical composition and electronic state of the nanocomposite (Fig. 3). For hematite sample, two peaks located at 710.9 eV and 724.2 eV with a spin-energy separation of 13.3 eV (Fig. 3A, curve a), corresponding to Fe^{3+} $2p_{3/2}$ and $2p_{1/2}$ of hematite as reported earlier. [51, 61] For the sintered α-Fe_2O_3, the XPS peak positions of Fe^{3+} $2p_{3/2}$ and $2p_{1/2}$ slightly positive shifted, suggesting that FeOOH existed in the sample transformed to hematite after calcination (Fig. 3A, curve b).[62] The similar shift of the position of the binding energy has also been observed for the other semiconductor systems, e.g. ZnO, after annealed under different temperatures.[63] Thus, all α-Fe_2O_3 used for preparing the nanocomposite is always calcined at 400 °C for 3 h. For α-Fe_2O_3/Mn_3O_4-1 hybrid, the binding energy of Fe 2p peaks increased about 0.26 eV compared with that of hematite (Fig. 3A, curve c), indicating the chemical interaction across the interface of hematite and Mn_3O_4.[64] The similar chemical shift also took place when TiO_2 was modified by WO_3.[65]
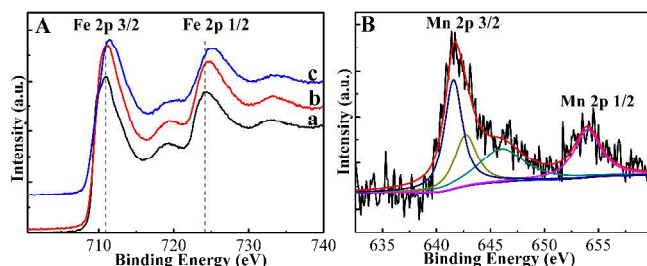

Fig. 3 High resolution XPS spectra of (A) Fe 2p from (a) α-Fe_2O_3, (b) α-Fe_2O_3 calcined under 400 °C and (c) α-Fe_2O_3/Mn_3O_4-1 samples; (B) Mn 2p from α-Fe_2O_3/Mn_3O_4-1 hybrid.

The high resolution XPS spectra of Mn 2p in α-Fe_2O_3/Mn_3O_4-1 hybrid are shown in Fig. 3B. The peaks at about 641.6 and 642.7 eV reveal that Mn^{2+} and Mn^{4+} exist in the sample.[66] Furthermore, the area ratio of two peaks is ca. 2:1, which is in good agreement with the theoretical value of Mn_3O_4. The weak peak situated at about 645.8 eV is belonged to the shakeup satellite peak of Mn^{2+} $2p_{3/2}$.[67, 68] The result provides new evidence that Mn_3O_4 has been decorated on the surface of hematite.

3.2. Light absorption and photoinduced charge transfer of the photocatalysts

Ultraviolet-visible diffuse reflectance spectroscopies of the samples are shown in Fig. 4A. Hematite demonstrates a robust absorption in UV-vis range from ca. 200 nm to 600 nm. The little bump at 558 nm is attributed to the weak indirect electron transition between Fe^{3+} d-d orbitals with different energy levels,[32] which are splitted by an intrinsic crystal field.[69] Moreover, a characteristic absorption peak appears at ca. 422 nm, which may be ascribed to the stronger direct charge transition from an O 2p

orbital to Fe 3d orbital.[32] For α-Fe_2O_3/Mn_3O_4-1 sample, a significant migration of the absorption edge to low energy region can be observed. The reduction of the band gap of the hybrid may attribute to forming a new energy level in the band structure of α-Fe_2O_3 since chemical bonds between hematite and Mn_3O_4 may have created. The analogous phenomenon has been observed in ZnS/Mn_3O_4 system.[70] For α-Fe_2O_3/Mn_3O_4-1/r-GO-3 sample, the enhanced absorption in whole region is due to the background absorption of r-GO, as reported previously.[3] Thus, the absorption ability of the photocatalysts with heterostructures has been greatly improved.
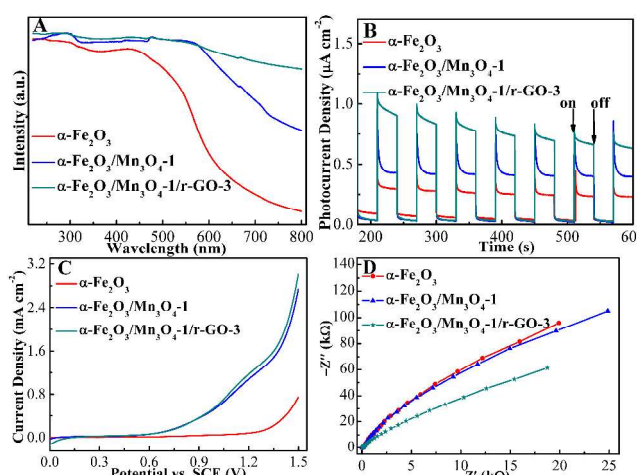

Fig. 4 (A) UV-visible diffuse reflectance spectra of the samples; (B) Photocurrent responses of the samples recorded at 0.5 V vs. SCE; (C) Linear sweep voltammetry plots of the samples scanning from 0 to 1.5 V vs. SCE; (D) Nyquist plots of electrochemical impedance spectra (EIS) for the samples. UV-visible light from a 150 W xenon lamp was used to irradiate electrodes which impregnated in 80 mL Na_2SO_4 aqueous solution (0.2 M, pH ~ 6).

Photocurrent test was performed to understand the electron transfer in the as-prepared samples (Fig. 4B). The weak photocurrent density (ca. 0.26 μA cm^{-2}) of α-Fe_2O_3/ITO electrode owes to the poor conductivity of hematite. The photocurrent density is up to 0.41 μA cm^{-2} when α-Fe_2O_3/Mn_3O_4-1/ITO is served as the work electrode. However, the photocurrent density of the α-Fe_2O_3/Mn_3O_4-1/r-GO-3/ITO electrode reached to 1.00 μA cm^{-2}. The great enhancement of the photocurrent for this electrode compared with other ones owes to the nice light absorption, the efficient electron transfer and charge separation of the α-Fe_2O_3/Mn_3O_4/r-GO nanocomposite.[71]

The linear sweep voltammetry plots of samples under UV-vis light irradiation are shown in Fig. 4C. For the electrode of α-Fe_2O_3/ITO, the onset potential is about 0.876 V vs. SCE, revealing the largish overpotential of hematite for oxygen evolution. For the electrode of α-Fe_2O_3/Mn_3O_4-1/ITO, the photocurrent rises steeply at about 0.468 V vs. SCE, negative shift about 408 mV compared with the onset potential of hematite, proving that the electrons in the electrode increased and the recombination rate of electron-hole pairs at the near flat band potential was reduced.[8] The similar phenomenon has also observed from Al_2O_3 modified hematite.[72] For the electrode of α-Fe_2O_3/Mn_3O_4-1/r-GO-3/ITO, the onset potential is almost the same as that of α-Fe_2O_3/Mn_3O_4-1/ITO but with higher

photocurrent, indicating more electrons are transferred to ITO through r-GO instead of recombination with holes on the surface of α-Fe$_2$O$_3$/Mn$_3$O$_4$-1 hybrid. Here r-GO acts as an electron acceptor and transporter because of its low energy level and the excellent electronic mobility.[73, 74]

Electrochemical impedance spectra (EIS) of the as-prepared photocatalysts presented as Nyquist plots are shown in Fig. 4D. The radius of Nyquist curves changes in the order of α-Fe$_2$O$_3$ > α-Fe$_2$O$_3$/Mn$_3$O$_4$-1 > α-Fe$_2$O$_3$/Mn$_3$O$_4$-1/r-GO-3, providing an order of the decrease of the resistance and the improvement of charge transfer at the interface of the electrode/electrolyte.[75] The similar phenomenon has also been observed from RuO$_2$ modified TiSi$_2$ electrode.[4] The small radius of Nyquist curve of α-Fe$_2$O$_3$/Mn$_3$O$_4$-1/r-GO-3 electrode implies the facile charge transfer with the help of r-GO and efficient hindrance of the charge recombination in the nanocomposite since the heterojunctions have been built.[76]
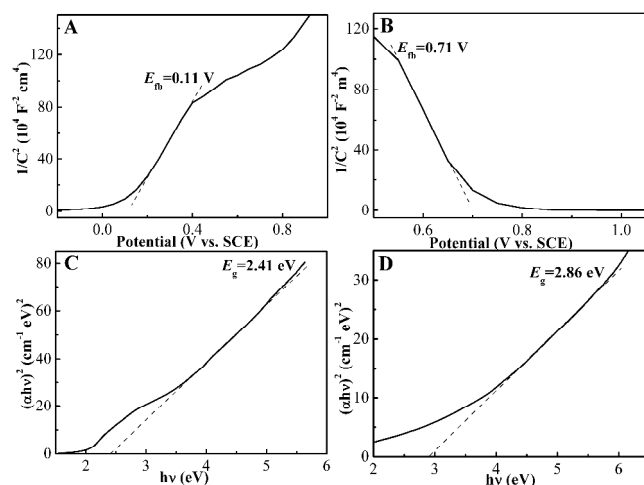

Fig. 5 Mott-Schottky plots of (A) α-Fe$_2$O$_3$ and (B) Mn$_3$O$_4$ were carried out in Na$_2$SO$_4$ solution (0.2 M, pH $\sim$ 6). Tauc plots of (C) α-Fe$_2$O$_3$ and (D) Mn$_3$O$_4$ for direct band gap.

In order to determine the relative band positions of main components in the nanocomposite, we measured flat band potentials and optical band gaps of α-Fe$_2$O$_3$ and Mn$_3$O$_4$, respectively, and the results are demonstrated in Fig. 5. The positive slope of the Mott-Schottky (M-S) curve in Fig. 5A suggests that hematite is a typical n-type semiconductor.[77] The observed flat band potential of hematite at the measured conditions is 0.11 V vs. SCE (0.71 V vs. RHE). For the sample of Mn$_3$O$_4$, the negative slope of M-S plot implies that Mn$_3$O$_4$ is a typical p-type semiconductor. As shown in Fig. 5B, the flat band potential of Mn$_3$O$_4$ is 0.71 V vs. SCE (1.31 V vs. RHE). The extrapolation of the Tauc plot on *x* intercepts gives the optical band gaps of 2.41 eV and 2.86 eV for α-Fe$_2$O$_3$ and Mn$_3$O$_4$ (Fig. 5C and D), respectively, which are close to the data reported by the literatures.[32, 78] Since the flat band potential of semiconductors may be considered approximately as valence band edge for p-type semiconductor and conduction band edge for n-type semiconductor,[79] the position of the conduction band edge for Mn$_3$O$_4$ and valence band edge for α-Fe$_2$O$_3$ is about -1.55 V vs. RHE and 3.12 V vs. RHE, respectively. Based on these data, the typical p-n heterojunction between α-Fe$_2$O$_3$ and Mn$_3$O$_4$ has been built and the potential diagram of the heterojunction

may be constructed as shown in Scheme 1. Under light irradiation, excited electrons are generated in both of the components of the hybrid electrode. Since the conduction band and valence band of α-Fe$_2$O$_3$ are more negative than the corresponding bands of Mn$_3$O$_4$, the photoinduced electrons in Mn$_3$O$_4$ move to the α-Fe$_2$O$_3$ side due to the potential difference, and then together with photoexcited electrons in α-Fe$_2$O$_3$ transfer to ITO. Such an ordered electrons flow promotes the separation of electron-hole pairs and enhances the photoconversion efficiency.
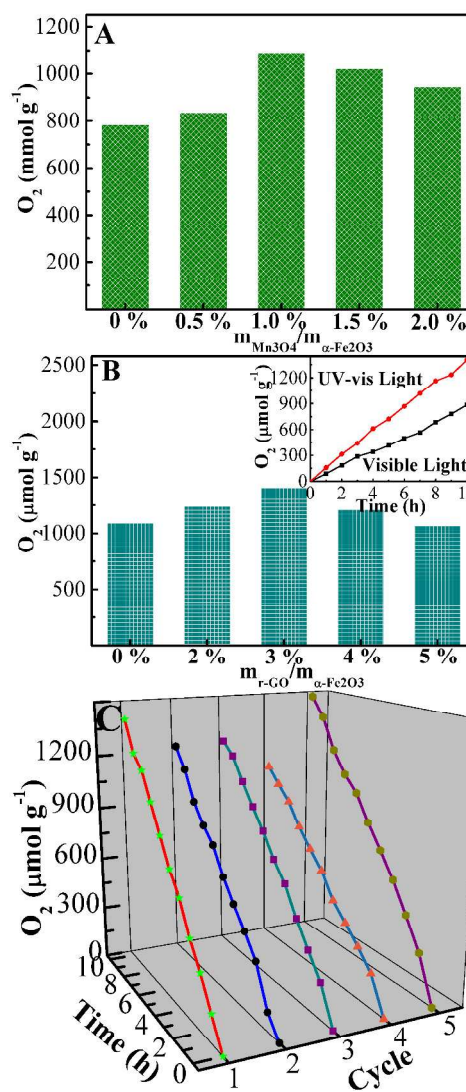
3.3. Photocatalytic oxygen evolution

Fig. 6 The amount of O$_2$ evolved by (A) hematite modified with different amount of Mn$_3$O$_4$ and (B) α-Fe$_2$O$_3$/Mn$_3$O$_4$-1 heterojunction modified with different amount of r-GO in 10 h UV-visible light irradiation, the inset of (B) is the curves of α-Fe$_2$O$_3$/Mn$_3$O$_4$-1/r-GO-3 under UV-visible and visible light irradiation, respectively; (C) The cycling experiments of oxygen evolution by α-Fe$_2$O$_3$/Mn$_3$O$_4$-1/r-GO-3 under UV-visible light irradiation. Reaction conditions: $c_{cat.}$ = 0.1 mg mL^{-1}, c_{KIO3} = 1.0 $\times$ 10^{-3} M, V = 50 mL, T = 298 K.

The blank experiment was carried out with 1.0 $\times$ 10^{-3} M KIO$_3$ aqueous solution irradiated by a 150 W GY-10 xenon lamp and only trace of oxygen could be detected. The photocatalytic results

of α-Fe$_2$O$_3$ and α-Fe$_2$O$_3$/Mn$_3$O$_4$ under 10 h UV-vis light irradiation are shown in Figure 6A. For hematite-catalysts calcined at different temperatures, the photocatalytic results demonstrate that the optimized calcination temperature is 400 °C.

5 The total amount of oxygen produced from α-Fe$_2$O$_3$ annealed at 400 °C is 781.8 μmol g^{-1}. Modification of hematite with Mn$_3$O$_4$ nanoparticles demonstrates positive effect on the enhancement of the photocatalytic activity. The amount of O$_2$ evolved from optimized α-Fe$_2$O$_3$/Mn$_3$O$_4$-1 hybrid catalyst is 1089.5 μmol g^{-1},

10 which is about 1.4 times as high as that of α-Fe$_2$O$_3$. The enhancement of photocatalytic activity of the hybrid catalyst is attributed to that efficient photoexcited electron transfer between two components hinders the charger recombination and also Mn$_3$O$_4$ performs as a site of water oxidation reduced the

15 overpotential of the reaction.[38] The photocatalytic results are in agreement with the outcomes of liner sweep voltammetry measurements. However, higher loading of Mn$_3$O$_4$ nanoparticles decreases photocatalytic activity since excess Mn$_3$O$_4$ might become the recombination centre of photogenerated charges.[80]

20 The excellent charge transmission ability of r-GO makes it useful as an electron mediator in photocatalytic system.[81] Cooperation r-GO with α-Fe$_2$O$_3$/Mn$_3$O$_4$-1 hybrid leads to great enhancement of the photocatalytic activity and the results are shown in Fig. 6B. Under UV-vis light irradiation for 10 h, α-

25 Fe$_2$O$_3$/Mn$_3$O$_4$-1/r-GO-3, with ca. a 2-fold enhancement of the photocatalytic activity (1406.2 μmol g^{-1}) compared with that of α-Fe$_2$O$_3$ and an apparent quantum yield of ~4.35 % at 365 nm, shows to be a high efficient catalyst for the photocatalytic oxygen evolution. The catalyst also demonstrates visible-light (λ > 400

30 nm) active for oxygen evolution from water. The amount of evolved oxygen was about 817.2 μmol g^{-1} after 10 h visible-light irradiation (Inset of Fig. 6B). However, overloading of r-GO leads to the decrease of the photocatalytic activity because of partial coverage of active sites by the overdose of r-GO.[82]

35 The stability of α-Fe$_2$O$_3$/Mn$_3$O$_4$-1/r-GO-3 was evaluated by performing the recycle experiments and the results are shown in Fig. 6C. About 1404.4 μmol g^{-1} of oxygen evolved in the first run under 10 h UV-vis light irradiation. The amount of evolved oxygen decreased slightly in the second cycle (1233.0 μmol g^{-1}).

40 This phenomenon has also been observed by other research group.[83] The activity of the catalyst did not change much in the third cycle (1243.5 μmol g^{-1}). The amount of oxygen produced from α-Fe$_2$O$_3$/Mn$_3$O$_4$-1/r-GO-3 reduced again (1178.0 μmol g^{-1}) in the fourth round. However, after 5.4 mL of KIO$_3$ solution (9.3

45 × 10^{-3} M) was added into the system, the amount of oxygen evolved from the catalyst was 1477.3 μmol g^{-1} in the fifth circulation. The total amount of O$_2$ produced from α-Fe$_2$O$_3$/Mn$_3$O$_4$-1/r-GO-3 is about 6426.6 μmol g^{-1} in the recycle experiments, and the average production rate of oxygen is about

50 128.3 μmol g^{-1} h^{-1}.

From the results of above, the proposed mechanism of photocatalytic water oxidation by α-Fe$_2$O$_3$/Mn$_3$O$_4$/r-GO nanocomposites are shown in Scheme 1. Under UV-vis light irradiation, α-Fe$_2$O$_3$/Mn$_3$O$_4$ hybrid was excited. The

55 photogenerated electrons in the conduction band of α-Fe$_2$O$_3$ transferred to r-GO to reduce IO$_3^-$ into I$^-$.[71] The electrons in conduction band of Mn$_3$O$_4$ transferred to conduction band of α-Fe$_2$O$_3$ due to the potential difference between them. The holes in

Mn$_3$O$_4$ immigrated to the surface and reacted with water to

60 produce oxygen.
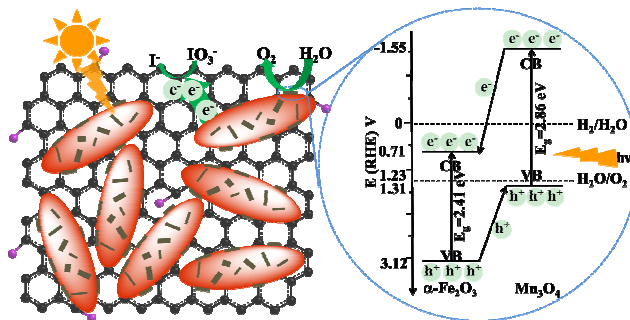
Scheme 1 Proposed mechanism of oxygen evolution from α-Fe$_2$O$_3$/Mn$_3$O$_4$-1/rGO-3 photocatalyst.

4. Conclusion

65

A novel nanocomposite consisted of α-Fe$_2$O$_3$, Mn$_3$O$_4$ and r-GO as a photocatalyst has been successively fabricated through solvothermal and self-assembly process. The α-Fe$_2$O$_3$/Mn$_3$O$_4$ hybrid prepared by modifying α-Fe$_2$O$_3$ with Mn$_3$O$_4$ nanoparticles

70 was proved well anchored on the two-dimensional r-GO sheets of the nanocomposite, resulting in the superior interfacial contacts between the hybrid and r-GO. The nanocomposite demonstrated high light-harvesting and photoconversion ability. The photocatalyst with the optimal composition showed much higher

75 photocatalytic performance for O$_2$ evolution under UV-vis or visible light irradiation. Such an enhanced photocatalytic activity could be attributed to the formation of heterostructures in the α-Fe$_2$O$_3$/Mn$_3$O$_4$/r-GO nanocomposite, which enhances photoinduced charge transfer and separation. Moreover, Mn$_3$O$_4$

80 in the nanocomposite can also act as the sites of water oxidation, reducing the overpotential of the reaction. This study displays an efficient method to construct a photocatalyst with heterostructures for enhancing photocatalytic activity.

Acknowledgements

Notes and References

a. College of Chemistry, Chemical Engineering and Materials Science, Soochow University, Suzhou 215123, China. Fax: +86 512 6588 0089; Tel: +86 512 6588 0361; E-mail: pyang@suda.edu.cn

95 *b. College of Chemistry and Bioengineering, Suzhou University of Science and Technology, Suzhou 215011, China*

c. CAS Key Laboratory of Colloid, Interface and Chemical Thermodynamics Institute of Chemistry, Chinese Academy of Sciences, Beijing 100190, China

100 † Electronic Supplementary Information (ESI) available: Fourier transform infrared (FTIR) spectra of (a) r-GO and (b) α-Fe$_2$O$_3$/Mn$_3$O$_4$-1/r-GO-3 nanocomposite. Raman spectra of (a) r-GO and (b) α-Fe$_2$O$_3$/Mn$_3$O$_4$-1/r-GO-3 nanocomposit. SEM images of (A) α-Fe$_2$O$_3$ and (B) α-Fe$_2$O$_3$

calcined under 400 °C. The corresponding characterizations of the samples of the spherical system. See DOI: 10.1039/b000000x/

1   X. Chen, S. Shen, L. Guo and S. S. Mao, *Chem. Rev.*, 2010, **110**, 6503-6570.
2   S. Martha, K. H. Reddy, N. Biswal and K. Parida, *Dalton Trans.*, 2012, **41**, 14107-14116.
3   Y. Chen, Z. Mou, S. Yin, H. Huang, P. Yang, X. Wang and Y. Du, *Mater. Lett.*, 2013, **107**, 31-34.
4   Z. Mou, S. Yin, M. Zhu, Y. Du, X. Wang, P. Yang, J. Zheng and C. Lu, *Phys. Chem. Chem. Phys.*, 2013, **15**, 2793-2799.
5   D. B. Grotjahn, D. B. Brown, J. K. Martin, D. C. Marelius, M.-C. Abadjian, H. N. Tran, G. Kalyuzhny, K. S. Vecchio, Z. G. Specht, S. A. Cortes-Llamas, V. Miranda-Soto, C. van Niekerk, C. E. Moore and A. L. Rheingold, *J. Am. Chem. Soc.*, 2011, **133**, 19024-19027.
6   H. Dau, C. Limberg, T. Reier, M. Risch, S. Roggan and P. Strasser, *ChemCatChem*, 2010, **2**, 724-761.
7   A. Iyer, J. Del-Pilar, C. K. King'ondu, E. Kissel, H. F. Garces, H. Huang, A. M. El-Sawy, P. K. Dutta and S. L. Suib, *J. Phys. Chem. C*, 2012, **116**, 6474-6483.
8   D. Wang, R. Li, J. Zhu, J. Shi, J. Han, X. Zong and C. Li, *J. Phys. Chem. C*, 2012, **116**, 5082-5089.
9   S. Chen, J. Yang, C. Ding, R. Li, S. Jin, D. Wang, H. Han, F. Zhang and C. Li, *J. Mater. Chem. A*, 2013, **1**, 5651-5659.
10 M. Grzelczak, J. Zhang, J. Pfrommer, J. Hartmann, M. Driess, M. Antonietti and X. Wang, *ACS Catal.*, 2013, **3**, 383-388.
11 X. Zong, C. Sun, H. Yu, Z. G. Chen, Z. Xing, D. Ye, G. Q. Lu, X. Li and L. Wang, *J. Phys. Chem. C*, 2013, **117**, 4937-4942.
12 R. Liu, Y. Lin, L.-Y. Chou, S. W. Sheehan, W. He, F. Zhang, H. J. M. Hou and D. Wang, *Angew. Chem. Int. Edit.*, 2011, **50**, 499-502.
13 D. K. Bora, A. Braun and E. C. Constable, *Energy Environ. Sci.*, 2013, **6**, 407-425.
14 S. Sakthivel, S. U. Geissen, D. W. Bahnemann, V. Murugesan and A. Vogelpohl, *J. Photoch. Photobio. A*, 2002, **148**, 283-293.
15 P. D. Tran, L. H. Wong, J. Barber and J. S. C. Loo, *Energy Environ. Sci.*, 2012, **5**, 5902-5918.
16 M. Liu, W. You, Z. Lei, G. Zhou, J. Yang, G. Wu, G. Ma, G. Luan, T. Takata, M. Hara, K. Domen and C. Li, *Chem. Commun.*, 2004, 2192-2193.
17 R. Abe, K. Shinmei, K. Hara and B. Ohtani, *Chem. Commun.*, 2009, 3577-3579.
18 J. W. Ko, W.-H. Ryu, I.-D. Kim and C. B. Park, *Chem. Commun.*, 2013, **49**, 9725-9727.
19 H. Huang, Z. Yue, Y. Song, Y. Du and P. Yang, *Mater. Lett.*, 2012, **88**, 57-60.
20 V. B. J. C. Cruz, S. Siracusano, V. Antonucci, A. S. Aricò, R. Ornelas, L. Ortiz-Frade, G. Osorio-Monreal, S. M. Durón-Torres, L.G. Arriaga, *Int. J. Electrochem. Sci.*, 2011, **6**, 6607-6619.
21 S. Zhu, N. Huang, H. Shu, Y. Wu and L. Xu, *Appl. Surf. Sci.*, 2009, **256**, 99-104.
22 T. Ohmori, H. Takahashi, H. Mametsuka and E. Suzuki, *Phys. Chem. Chem. Phys.*, 2000, **2**, 3519-3522.
23 K. Gurunathan, *Int. J. Hydrogen Energy*, 2004, **29**, 933-940.
24 X.-L. Wu, Y.-G. Guo, L.-J. Wan and C.-W. Hu, *J. Phys. Chem. C*, 2008, **112**, 16824-16829.
25 W. Hamd, S. Cobo, J. Fize, G. Baldinozzi, W. Schwartz, M. Reymermier, A. Pereira, M. Fontecave, V. Artero, C. Laberty-Robert and C. Sanchez, *Phys. Chem. Chem. Phys.*, 2012, **14**, 13224-13232.
26 Y. Shi, H. Li, L. Wang, W. Shen and H. Chen, *ACS Appl. Mater. Inter.*, 2012, **4**, 4800-4806.
27 S. Yang, Y. Xu, Y. Sun, G. Zhang and D. Gao, *CrystEngComm*, 2012, **14**, 7915-7921.
28 Y.-X. Zhou, H.-B. Yao, W.-T. Yao, Z. Zhu and S.-H. Yu, *Chem. Eur. J.*, 2012, **18**, 5073-5079.
29 L. S. Zhong, J. S. Hu, H. P. Liang, A. M. Cao, W. G. Song and L. J. Wan, *Adv. Mater.*, 2006, **18**, 2426-2431.
30 H. Yan, X. Su, C. Yang, J. Wang and C. Niu, *Ceram. Int.*, 2013, **40**, 1729-1733.
31 H. Liang and Z. Wang, *Mater. Lett.*, 2013, **96**, 12-15.
32 K. Sivula, F. Le Formal and M. Grätzel, *ChemSusChem*, 2011, **4**, 432-449.
33 T. Wang, M.-C. Huang, Y.-K. Hsieh, W.-S. Chang, J.-C. Lin, C.-H. Lee and C.-F. Wang, *ACS Appl. Mater. Inter.*, 2013, **5**, 7937-7949.
34 X. Yang, C. Du, R. Liu, J. Xie and D. Wang, *J. Catal.*, 2013, **304**, 86-91.
35 Y. Hou, F. Zuo, A. Dagg and P. Feng, *Nano Lett.*, 2012, **12**, 6464-6473.
36 D. K. Zhong and D. R. Gamelin, *J. Am. Chem. Soc.*, 2010, **132**, 4202-4207.
37 T. Hisatomi, H. Dotan, M. Stefik, K. Sivula, A. Rothschild, M. Grätzel and N. Mathews, *Adv. Mater.*, 2012, **24**, 2699-2702.
38 K. Maeda, A. Xiong, T. Yoshinaga, T. Ikeda, N. Sakamoto, T. Hisatomi, M. Takashima, D. Lu, M. Kanehara, T. Setoyama, T. Teranishi and K. Domen, *Angew. Chem. Int. Edit.*, 2010, **49**, 4096-4099.
39 Z. Li, Y. Chen, Y. Du, X. Wang, P. Yang and J. Zheng, *Int. J. Hydrogen Energy*, 2012, **37**, 4880-4888.
40 Z. Mou, Y. Dong, S. Li, Y. Du, X. Wang, P. Yang and S. Wang, *Int. J. Hydrogen Energy*, 2011, **36**, 8885-8893.
41 Y. Dong, Z. Mou, Y. Du and P. Yang, *Acta Chimica Sinica*, 2011, **69**, 2379-2384.
42 M. Zhu, P. Chen and M. Liu, *J. Mater. Chem.*, 2012, **22**, 21487-21494.
43 M. Zhu, P. Chen and M. Liu, *ACS Nano*, 2011, **5**, 4529-4536.
44 W. S. Hummers and R. E. Offeman, *J. Am. Chem. Soc.*, 1958, **80**, 1339-1339.
45 Y. Zhou, Q. Bao, L. A. L. Tang, Y. Zhong and K. P. Loh, *Chem. Mater.*, 2009, **21**, 2950-2956.
46 C.-J. Jia, L.-D. Sun, Z.-G. Yan, L.-P. You, F. Luo, X.-D. Han, Y.-C. Pang, Z. Zhang and C.-H. Yan, *Angew. Chem.*, 2005, **117**, 4402-4407.
47 M. Niu, F. Huang, L. Cui, P. Huang, Y. Yu and Y. Wang, *ACS Nano*, 2010, **4**, 681-688.
48 X. Li, L. Zhou, J. Gao, H. Miao, H. Zhang and J. Xu, *Powder Technol.*, 2009, **190**, 324-326.
49 J. L. Gunjakar, I. Y. Kim, J. M. Lee, N.-S. Lee and S.-J. Hwang, *Energy Environ. Sci.*, 2013, **6**, 1008-1017.
50 S. Bai, X. Shen, H. Lv, G. Zhu, C. Bao and Y. Shan, *J. Colloid Inter. Sci.*, 2013, **405**, 1-9.
51 S. Shen, J. Jiang, P. Guo, C. X. Kronawitter, S. S. Mao and L. Guo, *Nano Energy*, 2012, **1**, 732-741.
52 N. T. Hahn and C. B. Mullins, *Chem. Mater.*, 2010, **22**, 6474-6482.
53 R. Al-Gaashani, S. Radiman, N. Tabet and A. R. Daud, *J. Alloy. Compd.*, 2013, **550**, 395-401.
54 X. Zhou, J. Lan, G. Liu, K. Deng, Y. Yang, G. Nie, J. Yu and L. Zhi, *Angew. Chem.*, 2012, **124**, 182-186.
55 H. Xia, H. Zhuang, T. Zhang and D. Xiao, *Mater. Lett.*, 2008, **62**, 1126-1128.
56 H. Hu, Y. Liu, Q. Wang, J. Zhao and Y. Liang, *Mater. Lett.*, 2011, **65**, 2582-2584.
57 T. T. Baby, S. S. J. Aravind, T. Arockiadoss, R. B. Rakhi and S. Ramaprabhu, *Sensor. Actuat. B-Chem.*, 2010, **145**, 71-77.
58 Y. Ou, J. Lin, S. Fang and D. Liao, *Chem. Phys. Lett.*, 2006, **429**, 199-203.
59 G. Liu, Q. Deng, H. Wang, D. H. L. Ng, M. Kong, W. Cai and G. Wang, *J. Mater. Chem.*, 2012, **22**, 9704-9713.
60 D. P. Dubal and R. Holze, *RSC Adv.*, 2012, **2**, 12096-12100.
61 G. Rahman and O.-S. Joo, *Int. J. Hydrogen Energy*, 2012, **37**, 13989-13997.
62 Y. Ashok Kumar Reddy, A. Sivasankar Reddy and P. Sreedhara Reddy, *J. Alloy. Compd.*, 2014, **583**, 396-403.
63 R. K. Sahu, K. Ganguly, T. Mishra, M. Mishra, R. S. Ningthoujam, S. K. Roy and L. C. Pathak, *J. Colloid Inter. Sci.*, 2012, **366**, 8-15.
64 N. Bahadur, F. Kurayama, T. Furusawa, M. Sato, I. Siddiquey, M. M. Hossain and N. Suzuki, *J. Nanopart. Res.*, 2013, **15**, 1-11.
65 S. Stojadinović, N. Radić, R. Vasilić, M. Petković, P. Stefanov, L. Zeković and B. Grbić, *Appl. Catal. B-Environ.*, 2012, **126**, 334-341.
66 Y. Zhao, S. Nie, H. Wang, J. Tian, Z. Ning and X. Li, *J. Power Sources*, 2012, **218**, 320-330.
67 Y.-X. Zhang and Y. Jia, *New J. Chem.*, 2013, **37**, 3603-3606.
68 K. J. Kim, M.-S. Park, J.-H. Kim, U. Hwang, N. J. Lee, G. Jeong and Y.-J. Kim, *Chem. Commun.*, 2012, **48**, 5455-5457.

69   A. I. Galuza, A. B. Beznosov and V. V. Eremenko, *Low Temp. Phys.*, 1998, **24**, 726-729.

70   G.-J. Lee, A. Manivel, V. Batalova, G. Mokrousov, S. Masten and J. Wu, *Ind. Eng. Chem. Res.*, 2013, **52**, 11904-11912.

5 71   H. Huang, Z. Yue, G. Li, X. Wang, J. Huang, Y. Du and P. Yang, *J. Mater. Chem. A*, 2013, **1**, 15110-15116.

72   F. Le Formal, N. Tetreault, M. Cornuz, T. Moehl, M. Gratzel and K. Sivula, *Chem. Sci.*, 2011, **2**, 737-743.

73   S. Guo and S. Dong, *Chem. Soc. Rev.*, 2011, **40**, 2644-2672.

10 74   N. Zhang, Y. Zhang and Y.-J. Xu, *Nanoscale*, 2012, **4**, 5792-5813.

75   Y. Bai, J. Wu, J. Xi, J. Wang, W. Zhu, L. Chen and X. Qiu, *Electrochem. Commun.*, 2005, **7**, 1087-1090.

76   M. Zhu, Z. Li, B. Xiao, Y. Lu, Y. Du, P. Yang and X. Wang, *ACS Appl. Mater. Inter.*, 2013, **5**, 1732-1740.

15 77   A. Boudjemaa, S. Boumaza, M. Trari, R. Bouarab and A. Bouguelia, *Int. J. Hydrogen Energy*, 2009, **34**, 4268-4274.

78   A. U. Ubale, M. R. Belkhedkar, Y. S. Sakhare, A. Singh, C. Gurada and D. C. Kothari, *Mater. Chem. Phys.*, 2012, **136**, 1067-1072.

79   D. Hwang, J. Kim, T. Park and J. Lee, *Catal. Lett.*, 2002, **80**, 53-57.

20 80   X. Zong, J. Han, G. Ma, H. Yan, G. Wu and C. Li, *J. Phys. Chem. C*, 2011, **115**, 12202-12208.

81   Y. Sun, Q. Wu and G. Shi, *Energy Environ. Sci.*, 2011, **4**, 1113-1132.

82   Q. Li, B. Guo, J. Yu, J. Ran, B. Zhang, H. Yan and J. R. Gong, *J. Am. Chem. Soc.*, 2011, **133**, 10878-10884.

25 83   A. Iwase, Y. H. Ng, Y. Ishiguro, A. Kudo and R. Amal, *J. Am. Chem. Soc.*, 2011, **133**, 11054-11057.